Author/s:
Siu, PH;Karoly, PJ;Mansour L, S;Soto-Breceda, A;Kuhlmann, L;Cook, MJ;Grayden, DB

Title:
A neural mass modelling framework for evaluating EEG source localisation of seizure activity

Date:
2026-08-01

Citation:
Siu, P. H., Karoly, P. J., Mansour L, S., Soto-Breceda, A., Kuhlmann, L., Cook, M. J. & Grayden, D. B. (2026). A neural mass modelling framework for evaluating EEG source localisation of seizure activity. Journal of Neural Engineering, 23 (4), https://doi.org/10.1088/1741-2552/ae80fb.

Persistent Link:
https://hdl.handle.net/11343/370581

A neural mass modelling framework for evaluating EEG source localisation of seizure activity

Journal of Neural Engineering

OPEN ACCESS

RECEIVED
5 March 2026

REVISED
9 April 2026

ACCEPTED FOR PUBLICATION
23 June 2026

PUBLISHED
8 July 2026

PAPER

A neural mass modelling framework for evaluating EEG source localisation of seizure activity

Pok Him Siu[1,2,*], **Philippa J Karoly**[1,2], **Sina Mansour L**[1,3], **Artemio Soto-Breceda**[4], **Levin Kuhlmann**[5], **Mark J Cook**[1,2,6] **and David B Grayden**[1,2,6]

[1] Department of Biomedical Engineering, The University of Melbourne, Melbourne, Australia
[2] Graeme Clark Institute, The University of Melbourne, Melbourne, Australia
[3] National University of Singapore, Singapore, Singapore
[4] Grenoble Institut des Neurosciences, INSERM, Grenoble, France
[5] Department of Data Science & AI, Monash University, Melbourne, Australia
[6] Department of Medicine, St Vincent's Hospital, The University of Melbourne, Melbourne, Australia
[*] Author to whom any correspondence should be addressed.

E-mail: pokhim.siu@student.unimelb.edu.au

Keywords: neural mass model, Epileptor, EEG, source imaging, epilepsy

Supplementary material for this article is available online

Abstract

Objective. This study addresses the challenge of objectively evaluating electroencephalography and magnetoencephalography (EEG) source localisation algorithms in the absence of an experimentally verifiable ground truth, specifically for the characterisation of ictal dynamics. *Approach.* A simulation framework is presented for generating biologically plausible ictal dynamics and their corresponding EEG signals to enable systematic benchmarking of source imaging approaches. Cortical seizure initiation and propagation were simulated using network-coupled neural mass (Epileptor) models and combined with realistic forward models of the human head to produce macroscopic, electrophysiological data with known ground truth under varying conditions. *Main results.* Using this dataset, we evaluated the established MN-family of source localisation methods across idealised and realistic scenarios. Existing approaches achieved reasonable spatial accuracy under high-density, noise-free conditions, but performance degraded substantially with reduced sensor coverage and added noise. This degradation was driven primarily by failures to recover source polarity, even when spatial localisation remained relatively accurate. *Significance.* These results suggest that current methods may be sufficient for identifying epileptogenic regions or tracking regional recruitment but highlight polarity reconstruction as a key limitation for studies of seizure dynamics and network organisation. The proposed framework provides a reproducible and biologically grounded testbed for the development and evaluation of electrophysiological source localisation techniques.

1. Introduction

A pervasive problem with macroscopic, electrophysiological recordings electroencephalography magnetoencephalography (i.e. EEG/MEG) is that these measurements are a weighted sum of neural activity and, by themselves, do not directly define the underlying sources of neural activity. Implanted stereo-EEG (sEEG) electrodes are able to more directly measure this source activity, but are a highly invasive process and cannot cover the entire brain. Source imaging aims to recreate the neural activity of the underlying sources from the EEG/MEG data using mathematical techniques. However, the underlying problem remains that the sources estimated by these algorithms generally cannot be directly experimentally verified, making it difficult to evaluate and compare the effectiveness of different source imaging algorithms.

By introducing a realistic simulation of some underlying sources of neural activity with their corresponding EEG activity, a test set with a known

ground truth can be used to understand the differences between different source localisation methodologies and conditions. Previous studies have typically focused on one to a few sources of various spatial extents (Petrov 2012, Hecker *et al* 2021, Giri *et al* 2022, Cioppa *et al* 2023, Morik *et al* 2024, Rong *et al* 2025). However, such simplified source configurations provide limited biological plausibility given that the brain is known to be a highly interconnected and complex hierarchical structure (Eguíluz *et al* 2005, Burt *et al* 2018, Eickhoff *et al* 2018), capable of producing rhythmic and wavelike activity with wavelengths spanning several centimetres (Doelling and Assaneo 2021, Pang *et al* 2023, Koller *et al* 2024). Therefore, there remains a need for more adaptable ground-truth simulation frameworks to evaluate source imaging, specific to the application in mind.

Neural mass models are a class of physiologically informed dynamical models, capable of reproducing a diverse range of experimentally observed brain activity (Breakspear 2017, Siu *et al* 2022), such as seizures (Karoly *et al* 2018, Ying *et al* 2023), sleep (Costa *et al* 2016) and brain rhythms (Nunez 1974, Sotero *et al* 2007). Beyond replicating observable features of neural activity, these generative models of brain dynamics provide interpretable parameters that offer insight into the mechanisms that underlie specific brain phenomena (Karoly *et al* 2018, Maran *et al* 2025). Within epilepsy, a widely used example is the Epileptor model, which is a phenomenological dynamical model that has remarkable success in simulating seizure-like activity (Jirsa *et al* 2014). Studies have shown the ability of the Epileptor model to replicate not only many temporal features of seizure activity (Jirsa *et al* 2023, Wang *et al* 2023) but also spatial features of seizure activity, in that we can understand the spread of seizures in the brain (Moosavi *et al* 2022). Individualised models can be created and then used to identify seizure-causing regions of the brain and predict the outcome of different surgical interventions (Jirsa *et al* 2023, Wang *et al* 2023). The key distinction (and hence advantage) of a phenomenological model is that classification of seizure types through its parameters is based solely on the dynamic properties of the system, rather than assumptions on the underlying biophysical mechanisms (Houssaini *et al* 2020) as per other more physiological models. This is powerful, as epilepsy is believed to result from an instability of grey matter activity, observed consistently in humans and animals, even though the underlying pathological mechanisms often differ and remain unclear (Saggio and Jirsa 2024).

In addition to the phenomenological framework of the Epileptor, the biophysical modelling of epileptic activity has been extensively developed through lumped-parameter neural population models, such as the foundational Wendling model (Wendling *et al* 2000, 2002). The standard formulation of this model incorporates the nonlinear interactions between pyramidal cells and various interneuron populations (specifically excitatory, slow inhibitory, and fast inhibitory cells) to simulate the transition from interictal to ictal dynamics. This modelling approach was subsequently extended to construct physiologically plausible spatio-temporal frameworks for the simultaneous simulation of intracranial (Cosandier-Rimélé *et al* 2007) and scalp EEG signals (Cosandier-Rimélé *et al* 2008). These studies demonstrated that the observability (or lack thereof) of rapid discharges and epileptic spikes at the scalp is highly dependent on the location, spatial extent and synchrony of the underlying cortical sources, providing a link between depth-recorded activity and its representation on the scalp (Cosandier-Rimélé *et al* 2010, 2012). While these biophysical models offer detailed insights into the synaptic mechanisms of ictogenesis, the present study utilises the Epileptor's dynamic properties to focus on the macroscopic evolution of the seizure onset zone and its subsequent localisation.

Source localisation during epileptic seizures (ictal source localisation) has long been of interest due to its potential to non-invasively identify seizure-generating regions and to characterise the spatiotemporal recruitment of cortical networks during ictal events. Unlike interictal epileptic discharges, ictal activity evolves dynamically over time, spreads beyond the seizure onset zone, and often exhibits lower signal-to-noise ratios due to patient movement (van Mierlo *et al* 2020). Despite these difficulties, ictal source localisation offers important clinical advantages. The ultimate goal of epilepsy surgery is to eliminate the origin of seizures rather than interictal discharges, and these two phenomena do not necessarily have the same origin (Bartolomei *et al* 2016). By providing a more objective interpretation of scalp EEG than visual inspection alone, ictal source imaging can yield valuable localisation information to guide surgical resection or the placement of intracranial EEG electrodes (van Mierlo *et al* 2020). Consequently, accurate localisation of ictal sources is of high clinical relevance and has been increasingly investigated as a potential electrophysiological biomarker for the epileptogenic zone (Jiang *et al* 2025), providing a complementary perspective to interictal source imaging and other components of the epilepsy diagnostic pipeline.

This paper presents a framework for generating cortical simulations of ictal spread and their corresponding EEG/MEG signals. The key rationale is the need for an objective, repeatable methodology to determine the accuracy of source localisation approaches, with a focus on the minimum-norm family that dominates contemporary clinical EEG/MEG practice (van Mierlo *et al* 2020). These simulations aim to answer the following questions:

1. How do different modelling parameters and decisions affect what we see at the source (neural) level as well as the macroscopic EEG/MEG level?
2. Are these simulations able to serve as a useful source of truth to benchmark source imaging algorithms?
3. How well can existing source localisation methods recreate pathological brain activity?

2. Methods

2.1. Epileptor model

This study used a common implementation of the Epileptor model, as implemented in the virtual brain project (TVB) (Sanz-Leon *et al* 2015), where the dynamical behaviour of epileptic seizures is characterised using five state variables (x_1, y_1, x_2, y_2, z), a dummy variable (u) within region i, and an input variable J_i representing the excitatory input into region i from all other regions (Jirsa *et al* 2017). Table 1 summarises the Epileptor state variables and model parameters. The Epileptor equations are

$$\tau_1 \dot{x}_1 = y_1 - f_1(x_1, x_2, z) - z + I_{\text{rest},1}, \quad (1a)$$

$$\dot{y}_1 = y_0 - 5x_1^2 - y_1, \quad (1b)$$

$$\tau_0 \dot{z} = 4(x_1 - x_0) - z + J_i, \quad (1c)$$

$$\dot{x}_2 = -y_2 + x_2 - x_2^3 + I_{\text{rest},2} + 2u - 0.3(z - 3.5), \quad (1d)$$

$$\tau_2 \dot{y}_2 = -y_2 + f_2(x_2), \quad (1e)$$

$$\dot{u} = -\gamma(u - 0.1x_1). \quad (1f)$$

where

$$f_1(x_1, x_2, z) = \begin{cases} x_1^3 - 3x_1^2, & x_1 < 0, \\ \left(x_2 - 0.6(z-4)^2\right) x_1, & \text{otherwise}, \end{cases} \quad (2a)$$

$$f_2(x_2) = \begin{cases} 0, & x_2 < -0.25, \\ 6(x_2 + 0.25), & \text{otherwise}, \end{cases} \quad (2b)$$

$$\tau_{ij} = \frac{D_{ij}}{v}, \quad (2c)$$

$$J_i = -g \sum_{j=1}^{N} W_{ij} \left[x_{1,j}(t - \tau_{ij}) - x_{1,i}(t)\right]. \quad (2d)$$

Representation as Dipoles

The Epileptor model generates time series representing dimensionless neural activity within a single region of the brain. To represent extracellular dipoles (x), the Epileptor equations were modified to

$$x = (x_1 - x_2 - b)/n \times 10^{-5}, \quad (3)$$

where $x_1 - x_2$ was used instead of $x_2 - x_1$, as by Jirsa *et al* (2014), to ensure that the seizure state has a positive orientation, n is the number of dipole sources in the source space, and 10^{-5} converts to the physical units of A · m, consistent with the standard SI representation of neural current sources. In this formulation, b is a baseline constant, subtracted from the Epileptor model, to ensure that dipole sources maintain approximately zero baseline

Table 1. Table of variables and parameters of the Epileptor

	State variables	Interpretation
	$x_1(t), y_1(t)$	Fast timescale rapid discharges
	$x_2(t), y_2(t)$	Intermediate timescale spike-and-waves
	$z(t)$	Slow timescale transition between seizure and non-seizure
	Other variables	
	$u(t)$	Dummy variable for low-pass filtering from x_1 to x_2
	$J_i(t)$	Coupling term describing total input into region i from all other regions
	Adjusted parameters	
x_0	$-2.1 \rightarrow -1.6$	Node excitability
g	$1.5 \rightarrow 2.0$	Global coupling strength
W_{ij}	$0.0 \rightarrow 1$	Coupling weights defined by SCM into region i from j
D_{ij}	$0.0 \rightarrow 248.5$	Streamline lengths between regions (mm)
τ_{ij}	$0.8 \rightarrow 82.8$	Time delays between regions (ms)
	Fixed parameters	
$I_{\text{rest},1}$	3.1	Constant injection current for x_1
$I_{\text{rest},2}$	0.45	Constant injection current for x_1
y_0	1	Threshold constant for y_1
γ	0.01	Time constant of low-pass filter
τ_1	1	Time constant of of fast activity
τ_2	10	Time constant of spike-and-waves
$r = 1/\tau_0$	0.000 15	Temporal scaling of long timescale activity
v	3	Axon conduction velocity (ms^{-1})
σ^2	0.0001	Stochastic noise term (variance) affecting frequency of inter-ictal spikes and seizures

activity, as expected from the Debye shielding of ions in the electrolyte solution of the extracellular space (Nunez and Srinivasan 2006).

Coupled neural mass models for seizure spread

To generate seizure activity across the brain, this study used simulations of coupled masses of Epileptor models, as defined in equation (1), through the coupling current J_i. In this framework, each neural mass model corresponded to one cortical or subcortical region according to the Yan 1000 cortical parcellation atlas (Yan *et al* 2023). The connectivity weight matrix (W_{ij} in equation (2*d*)) was therefore defined by the structural connectome of an exemplar human subject (see section 2.2). The axonal time delays τ_{ij} were defined by the 1019 region connectome streamline lengths (D_{ij}) divided by a conduction speed of 3 m s^{-1} (Sanz Leon *et al* 2013).

A Heun's stochastic integrator was used with Gaussian additive noise ($\sim N(0,\sigma^2)$) added to the variables x_2 and y_2 (Jirsa *et al* 2014, Moosavi *et al* 2022). An integration step-size $\Delta t = 0.05$ was used. To match the temporal properties of focal seizures, the timescale of the model output was scaled such that 256 time steps correspond to 1 s, as similar to Jirsa *et al* (2017). Seizure simulations were set to have a 1 min duration to allow sufficient ictogenic activity to develop. To generate each simulation, a single given region (i.e. represented by one Epileptor model) was first defined as the 'epileptogenic zone'. All regions other than the epileptogenic zone were set to have an excitability of $x_0 = -2.1$; i.e. tuned to be at the cusp of a bifurcation (Houssaini *et al* 2020, Moosavi *et al* 2022). To trigger a seizure, the excitability x_0 for the specified epileptogenic zone was increased to -1.6. The global coupling strength was set at $g = 1.5$ or $g = 2$ to obtain two different degrees of seizure spread.

In total, 2038 simulations were generated to produce a dataset with variations in seizure morphology by changing the specified epileptogenic zone and the global coupling strength. The carpet plots of figure 1(a) and figure S4 depict the seizure propagating across the simulated brain regions. With higher coupling strength ($g = 2$), all simulations produced seizures that spread throughout all brain regions (as in figure 1) . Intermediate coupling ($g = 1.5$) produced seizures that only partially spread through the brain in the 1 min seizure duration (as in figure S4). Partial seizure spread occurred as a result of three effects of lower connectivity strength: i) reduced gain in external current between regions, ii) slower region recruitment, and iii) the refractory period of each region (preventing too many regions from undergoing a seizure together). The result is a lower net current between regions, meaning that some regions never receive enough current to drive a transition into a seizure state.

2.2. Structural brain data

Structural brain data from the human connectome project (HCP) (Van Essen *et al* 2013) was used, with HCP Subject 100 206 (HCP100206) chosen as the primary subject for this work. The T1 MRI image with the skull included was used to generate surface meshes in the subject's native space for the skin, skull, and cortex using freesurfer's recon-all (Fischl 2012). The individual subject's cortical mesh was aligned to the fsaverage template mesh, which consisted of 163 842 vertices per hemisphere.

Parcellation Atlas Each vertex was attributed to one of the cortical regions of a specified parcellation atlas. Three cortical parcellations were considered: the Yan 1000 region homotopic atlas (Yan *et al* 2023), the Glasser 360 region atlas (Glasser and Van Essen 2011), and the Desikan–Killiany 68 region atlas (Desikan *et al* 2006). The Yan 1000 atlas was selected because its finer parcels provide a more direct correspondence between neural mass simulations and dipole source space, avoiding the overly large cortical patches produced by coarser parcellations. The location of each cortical region was defined as the centroid of its vertex coordinates. In addition to the 1000 cortical regions, 19 subcortical structures defined by the cifti grayordinate template (Glasser *et al* 2013) were also included, resulting in a 1019-region parcellation of the entire brain.

Structural Connectome The individual's structural connectome was computed via a diffusion MRI tractography pipeline detailed in previous work (Mansour *et al* 2021, 2023) using the MRtrix3 software (Tournier *et al* 2019). The fibre orientation distributions (FODs) were computed from tissue-specific response functions via Multi-Shell Multi-Tissue Constrained Spherical Deconvolution (Jeurissen *et al* 2014, Dhollander *et al* 2016). A total of 5 million tractography streamlines were estimated by an anatomically constrained probabilistic tractography algorithm based on second-order integration over FODs (Tournier *et al* 2010, Smith *et al* 2012). Notably, streamlines were randomly seeded from the grey matter white matter interface. A radial search with a maximum radius threshold of 4 mm was used to map streamlines to the regional parcellation, resulting in a 1019×1019 connectivity matrix of streamline counts. The matrix of streamline counts was then normalised by the maximum streamline count to end in a normalised connectivity matrix with entries between 0 and 1. In addition, a 1019x1019 streamline length matrix was computed to quantify average streamline lengths between all pairs of connected regions. To obtain the group-averaged connectivity matrix of streamline counts, the sum of streamlines between regions was taken for

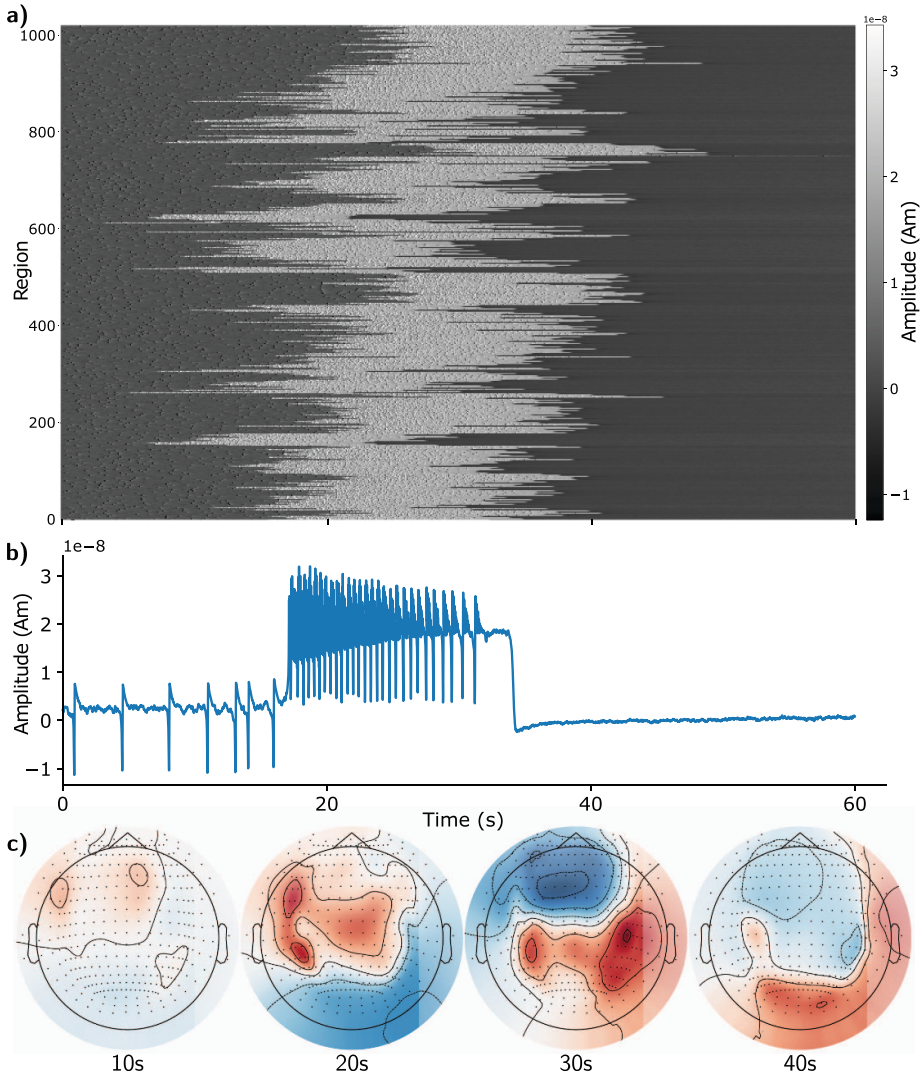

Figure 1. Epileptor model seizure originating from the left temporal pole. (a) Carpet plot (Siu *et al* 2022) of a simulated seizure originating in the left temporal pole with coupling strength $g = 2$. White regions indicate high-amplitude epileptiform activity. At this coupling level, seizure dynamics propagate across the entire brain network. (b) Representative Epileptor time series showing key seizure features: interictal spikes (~ -10 nAm), spike–wave discharges ($\sim$20 nAm) with a DC shift, and a postictal refractory period without interictal spikes. The Epileptor equations were adjusted (equation (3)) so that baseline activity is centred near zero and seizure activity appears positive. (c) Example EEG scalp topography obtained by projecting the source activity in panel a to sensor space using the forward model (equation (4)).

every patient, and the aggregate matrix is normalised between 0 and 1.

Dipole Source Space The dipole source space is a representation of all dipole neural sources, located on the cortical surface, which can be summed to generate EEG/MEG data. These dipoles are nominally oriented normal to the cortical surface, but some flexibility can be allowed for the orientation to be 'loose' and deviate slightly from the normal. In this work, a discrete source space was used where the centre of each cortical region of the Yan 1000 parcellation was approximated as a dipole. Seizure (Epileptor neural mass model) simulations were mapped directly (1-to-1) to the source space based on the cortical parcellation of the subject.

2.3. Mapping to sensor space with MNE Python

Having generated simulated activity at the mesoscopic source level of brain regions, these simulated sources were then mapped to their corresponding signals in EEG/MEG sensor space using using OpenMEEG's (Gramfort *et al* 2010) implementation of the boundary element method (BEM) for the forward problem with the corresponding forward model for the subject. Under the quasi-static assumption (Hallez *et al* 2007, He *et al* 2018), this transformation can be described by the linear model

$$y = Fx + \epsilon, \tag{4}$$

where the transformation matrix $F \in \mathbb{R}^{M\times N}$ (known as the forward matrix or lead field matrix) maps any

neural activity in source space $x \in \mathbb{R}^{N\times T}$ to sensor space $y \in \mathbb{R}^{M\times T}$. The dimensions represent the number of sensors (M), the number of possible sources in the brain (N), and the number of time steps (T), while ϵ is a matrix that represents the overall measurement noise for each time step. For the purposes of EEG source localisation, the quasi-static condition holds true, as it has been shown that charge does not accumulate in the extracellular space for the frequency range of signals measured with EEG (Hallez *et al* 2007), meaning that, for each instance in time, all electric and magnetic fields are dependent only on the active electric source (Nunez and Srinivasan 2006). The BEM model consisted of three concentric layers, with standard conductivity values assigned as: 0.3 S m^{-1} (skin), 0.006 S m^{-1} (skull), and 0.3 S m^{-1} (cortex) (Gramfort *et al* 2014). The number of sensors varies depending on the EEG-spacing montage used, such that 10–20 spacing involves 21 electrodes, 10–10 spacing involves 88 electrodes, 10–05 spacing involves 339 electrodes. A visualisation of the sensors, dipole sources, and head surfaces can be found in figure S8.

To simulate the challenge of measurement noise contamination, Gaussian white noise was added to the EEG signal with signal-to-noise-ratios (ρ) of 3 dB, 10 dB, or None (signifying that no white noise was added). The standard deviation of the noise is given by

$$\sigma_{\text{Noise}} = \frac{P_{\text{Signal}}}{\sqrt{10^{\frac{\rho}{10}}}}. \tag{5}$$

During the source inversion stage, the regularisation parameter (α or λ^2) was set to $10^{-\rho/10}$, based on a heuristic.

2.4. Performance metrics

To assess the accuracy of source localisation within simulations, the following evaluation metrics were used.

Cosine score S_C

$$S_C = \frac{\hat{x}\cdot x}{||\hat{x}||||x||}, \tag{6}$$

where x is the true signal and $\hat{x}$ is the source estimate. Dependent on the figure, S_C was presented for each time point or averaged across time. The cosine score captures relative distributional accuracy, reflecting how well the relative pattern of activation across the source space matches the true activity.

Normalised residual sum of squares nRSS

$$\text{nRSS} = \sum_i \left(\frac{\hat{x}}{\max(|\hat{x}|)} - \frac{x}{\max(|x|)}\right)^2, \tag{7}$$

where the data was normalised using the maximal value, to compare across methods with differing units.

Mean squared error MSE

$$\text{MSE} = \frac{1}{N}\sum_i \left(\frac{\hat{x}}{\max(|\hat{x}|)} - \frac{x}{\max(|x|)}\right)^2 = \frac{nRSS}{N}, \tag{8}$$

where $N = 1000$ is the number of dipole sources.

Variance explained R^2

$$R^2 = 1 - \frac{\Sigma_i(\hat{x}-x)^2}{\Sigma_i x^2} = 1 - \frac{\text{nRSS}}{\text{nSS}}, \tag{9}$$

where nRSS is the normalised residual sum of squares and nSS is the normalised sum of squares over all possible sources i in source space. Note that for the simulated signals used here, a baseline constant was already identified and subtracted (see equation (3)) such that the baseline for x is at 0.

Region localisation error *RLE*

$$RLE = \frac{1}{2Q}\sum_{k\in I}\min_{l\in\hat{I}}||r_k - r_l|| + \frac{1}{2\hat{Q}}\sum_{l\in\hat{I}}\min_{k\in I}||r_k - r_l||, \tag{10}$$

where I and $\hat{I}$ represent the true and estimated indices of active sources, respectively, Q and $\hat{Q}$ represent the number of true and estimated active sources, and r_k denotes the position of the kth dipole source in space as per MNE-Python's implementation (Gramfort *et al* 2014). Sufficiently active sources were algorithmically identified to be those beyond Otsu's Threshold (Otsu 1979) as suggested by Sun *et al* (2022, 2024). The region localisation error was computed across time, as well as at 50% of maximum EEG power, representing a sensible extent of seizure spread and the rising phase of a seizure (Plummer *et al* 2019). Region localisation error captures spatial accuracy, reflecting how precisely the estimated source activity is positioned in space.

2.5. Source localisation algorithms

Having created plausible simulations of seizure spread at both the sensor and source levels, the simulations were used to evaluate the performance of four current source localisation approaches. These algorithms were implemented in MNE-Python and fall under the MN-family of source localisation algorithms, consisting of MNE (Hämäläinen and Ilmoniemi 1994) (classical minimum L2 norm estimation), dSPM (Dale *et al* 2000) (MNE with posthoc noise normalisation), sLORETA (Pascual-Marqui *et al* 2002) (MNE with source-covariance normalisation), and eLORETA (Pascual-Marqui 2007) (MNE with minimum localisation error weighting). All methods used an identical forward model, source space, depth, orientation, and regularisation parameters such that differences in performance reflected the inverse solution alone.

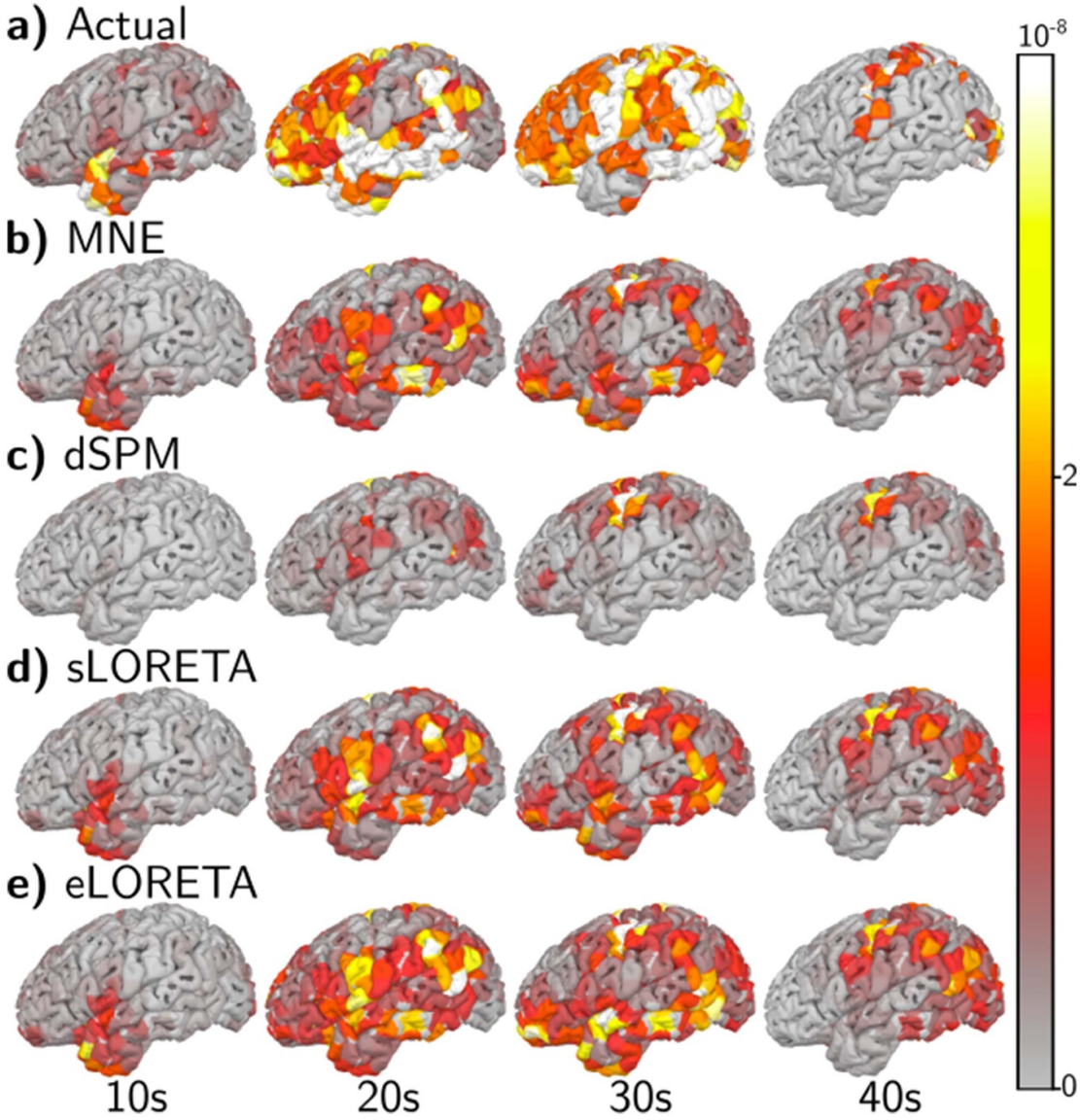

Figure 2. MN-family estimates for seizure originating from left temporal pole plotted on left hemisphere. The colour scale represents source amplitude, with white indicating the maximum amplitude and transitioning through yellow, orange, and red to transparent at zero. (a) Ground-truth source activity generated using the Epileptor model. As the simulation progresses, seizure activity propagates from anterior to posterior brain regions. During this period, different cortical areas become active with varying spatial extents and patterns. (b)–(e) Algorithms from the MN-family predict more focal sources with regularisation parameter set according to the $10^{-\rho/10}$ heuristic. For visualisation and to improve performance, the orientation of the dipole was allowed to be loose for the MN-family, which we demonstrate to be near equivalent to taking the absolute value of a fixed orientation estimate.

3. Results

In total, 2038 simulations were generated to produce a dataset with variations in seizure morphology by changing the specified epileptogenic zone (1019 possible regions) and the global coupling strength (two possible values). Figure 2 provides a visual representation of the abilities of the MN-family to recreate the propagation of an example seizure simulation originating from the left temporal pole with coupling strength $g = 2$. The following sections outline insights into the performance of the four source localisation algorithms compared.

3.1. Existing approaches are challenged by irregular sources

For a more direct comparison with previous literature, which usually focuses on one or a few sources of various extents (Petrov 2012, Hecker *et al* 2021, Giri *et al* 2022, Cioppa *et al* 2023, Morik *et al* 2024, Rong *et al* 2025), we computed a simple set of single-source simulations. These sources were generated with varying sizes such that, for each simulation, one cortical region of the 1000-region parcellation was selected as the centre. Regions within a certain radius were then selected as part of the entire patch. This simulation would also be more similar to the case of averaged interictal spikes.

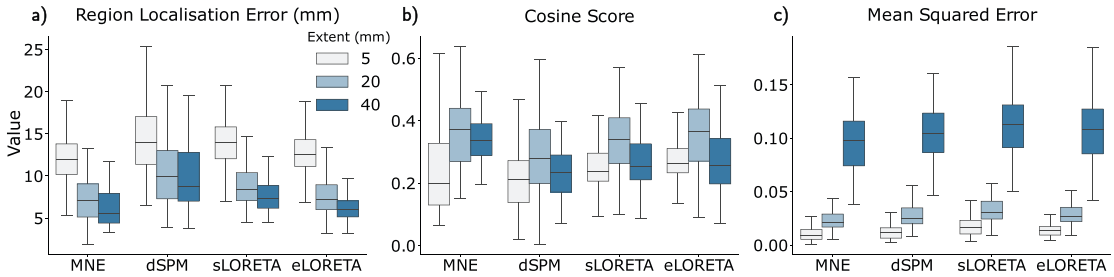

Figure 3. Single patch source localisation metrics. Source localisation results for varying extents were computed for off-the-shelf algorithms from MNE-Python. A 10–10 montage with 88 EEG electrodes was used. The box range shows the interquartile range and the median. Each subfigure graphs a different metric: (a) region localisation error, (b) cosine score, (c) mean squared error. Each hue represents underlying sources of different extents (radius of 5 mm, 20 mm, 40 mm).

Figure 3 shows the performance metrics for existing, 'off-the-shelf' source localisation methods. The region localisation error of approximately 0.5–2 cm (figure 3(a)) was consistent with previous findings (Sohrabpour *et al* 2020, Hecker *et al* 2021, Hauk *et al* 2022, Sun *et al* 2022). Interestingly, the reduction in region localisation error and the increase in mean squared error indicate that reconstruction accuracy declines as the spatial extent of the source increases. This behaviour is likely driven by the way extended patches were generated; as patch size grows, the resulting sources become less circular and develop increasingly irregular boundaries (see figure S7). The minimum-energy constraints inherent to MN-family algorithms are biased against irregular shapes and instead favour compact, smoothly distributed sources. Furthermore, larger patch sizes mean that sources encompass more areas of cortical curvature, producing cancellation when dipole normals are oriented in opposite directions. We also observe point-spread artefacts (i.e. spatial 'ringing') and smoothing effects in figure S7, which are well-known and typically undesirable features of MN-family inverse solutions (Hauk *et al* 2022).

3.2. Increasing the number of electrodes allows polarity to be resolved

Figure 4 shows the source localisation metrics across the simulated dataset, where the variable parameters were signal-to-noise ratio, number of electrodes, and algorithms. The previous section discussed the challenge of irregular and widespread sources for existing algorithms. This challenge is further evidenced by figure 4(d), columns 2 and 3 (representing the EEG 10–10 and 10–20 montages, respectively). At 21 and 88 electrodes, the MN-family of methods was unable to accurately determine the polarity of sources, as evidenced by the variances explained being close to 0 and the relatively low cosine scores. At 343 electrodes, the MN-family was able to resolve the polarity of sources, leading to substantial increases in performance/accuracy. The estimation of polarity is discussed in more detail in Results section 3.4 and Discussion section sec:sim_polarity_discussion.

Considering the RLE at 50% of EEG power (figure 4(b)), performance appeared stable across electrode configurations at approximately 6 mm on average. This RLE signifies the reasonable spatial accuracy of the source localisation algorithms, and is in line with previous findings of (Sharma *et al* 2019, Hecker *et al* (2021), Pascarella *et al* (2023)). The RLE showed that the best results were obtained with no noise, and SNRs of 10 and 3 showed minimal differences after regularisation. dSPM performed poorly relative to the other algorithms for this metric, except for electrode configuration 10–20.

In terms of cosine score (figure 4(c)) and variance explained (figure 4(d)), both follow similar qualitative trends given that they are closely related metrics. The distinction is that variance explained has a wider dynamic range and is sensitive to both magnitude and alignment, whereas cosine score is bounded and, therefore, less sensitive to variation at higher ($\sim$1) and lower ($\sim$0) performance levels, and does not consider magnitude. Under noisy conditions or montages with 88 or fewer electrodes, the metrics indicate poor localisation results.

Overall, the mean squared error (figure 4(e)) was shown to increase by approximately 30% from no noise to 10 dB noise, with only a slight further increase from 10 dB to 3 dB for the 10-05 montage. These jumps in error as noise increased were less pronounced for simulations with fewer electrodes, likely because the baseline errors (in noise-free conditions) were already higher. This pattern, where the error increases quickly and then plateaus, likely signifies a saturation in error.

3.3. Localisation error varies throughout the seizure

Figure 5 illustrates that region localisation error varies throughout a seizure, following a characteristic temporal profile. Immediately before and during the initial recruitment of seizure activity (0–10 s), the RLE is relatively high with substantial variability, indicating reduced confidence and stability in the source localisation estimate during the initial distributed activation. As the seizure evolves into the mid phase

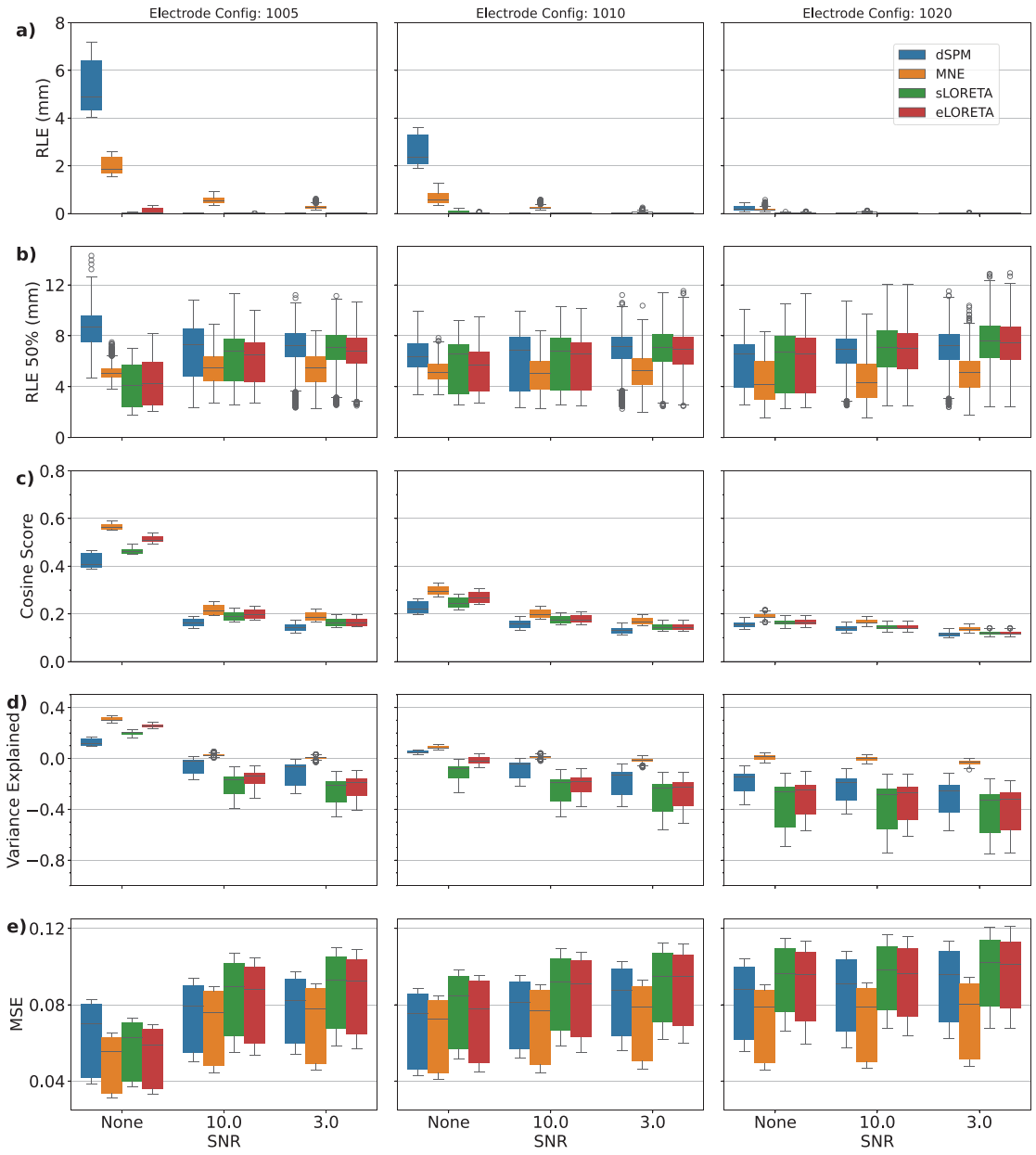

Figure 4. MN-family source localisation metrics. Each algorithm from the MN-family is represented by a different colour: dSPM (blue), MNE (orange), sLORETA (green), and eLORETA (red). Each row, labelled a–e, displays a different metric: region localisation error, region localisation error at 50% of EEG max power, cosine score, variance explained, and mean squared error. Each column corresponds to a different electrode configuration: '10–05', '10–10', and '10–20' spacing. Within each sub-figure, the *x*-ticks represent the signal-to-noise ratio: none (no noise), 10 dB, and 3 dB. Metrics are computed with a 'fixed' orientation, meaning that dipoles are assumed to be oriented perpendicular to the cortical surface.

(defined as when 50% of maximum EEG power is reached (Plummer *et al* 2019), typically occurring at around 10–20 s into the simulations), the localisation error decreases markedly and remains at its lowest level during the sustained ictal period (around 20–40 s). This indicates that source localisation becomes more stable when the spike waveforms are better established and the signal-to-noise ratio is stronger. Toward the end of the seizure (>50 s), the RLE increases again, consistent with the broader spatial dispersion and complex propagation patterns in late ictal dynamics. Overall, these results suggest that the mid-ictal stage provides the most reliable signal for source localisation, whereas both early recruitment and late spread reduce localisation accuracy due to rapidly changing and irregular source configurations.

3.4. Effect of dipole orientations

Allowing the orientation of the dipoles to be free to deviate from the normal of the cortical surface (also referred to as loose orientation) is a common approach in source localisation (Lin *et al* 2006, Gramfort *et al* 2014). In this work, the dipoles were oriented normal to the cortical surface for the simulation. However, as shown in figure 6 and figure S5, allowing a deviation from the normal of the cortical

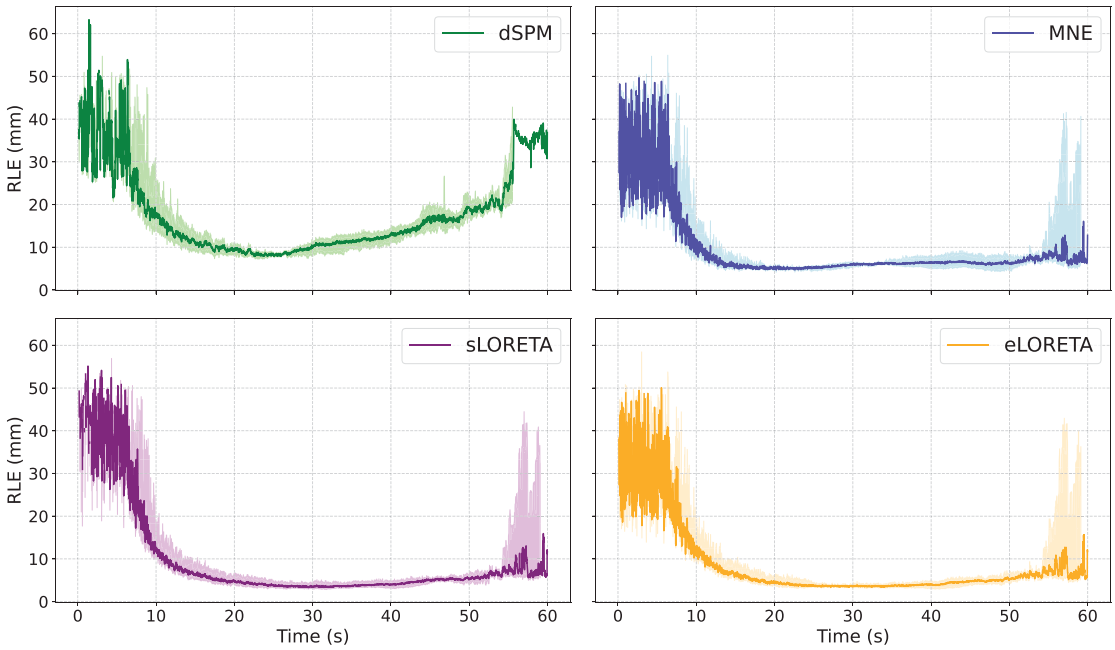

Figure 5. Region localisation error over time for algorithms in the MN-family. The solid line shows the median region localisation error and the shaded region indicates the interquartile range across simulations. The mid-phase of a seizure is defined to start when 50% of maximum EEG power is reached, typically occuring at around 10–20 s into the seizure, depending on the simulation. Otsu's threshold was used for calculating RLE shown, but the results remained consistent across thresholds from 10% to 60% for a SNR of 10.

surface, by enabling the dipole deviation to be greater than zero, increased performance for all source localisation methods. The standard explanation would be that the loose orientation provides extra degrees of freedom to account for small errors with the forward model, mesh discretisation, downsampling, etc. To test if this is the case, we consider the effects of different variations of implementing loose vs. fixed orientation using the eLORETA algorithm, as shown in figure 6. Sequentially, the shades of blue represent fixed orientation, and the warm colours represent settings of loose orientation.

In figure 6, comparing the fixed orientation (light blue) with loose orientation (gold) demonstrates how setting a loose orientation significantly improves source localisation performance, with mean squared error reducing from 0.077 to 0.048 under no noise conditions. However, the gold boxplot demonstrates that the performance increase can also be seen by simply taking the absolute value of the fixed orientation estimate. Further increase of the loose parameter (comparing gold to orange) appears to only slightly increase the performance for eLORETA, with mean squared error improving from 0.052 (gold: loose $=$ 0.05) to 0.048 (orange: loose $=$ 1) under no noise conditions. Essentially, what this means is that the removal of the direction (and only taking the magnitude) produces the bulk of the performance increase, rather than the allowance of deviation to the cortical surface. Indeed, the mahogany boxplot displays the estimate and metric when only considering the orientation component normal to the surface results in relatively poor performance. This is supported by region localisation error, a polarity agnostic measurement, remaining relatively stable across changes to the loose parameter. This is not necessarily a flaw with loose orientation, but an artefact of vector estimation. After finding the loose source estimate, there is a need to compare it with the true source, which is oriented normal to the cortical surface. The typical method used to compare the estimated with true sources, which is the default in MNE-Python, is to condense the vector into a magnitude and compare metrics, and this is what was performed to generate the results for the loose orientations in figure 6 (warm colours).

4. Discussion

This study introduced a benchmarking framework for source localisation algorithms using simulated seizures to evaluate performance against known onset regions. Simulations were able to capture key features of clinical epileptic seizures in both the source space and the resulting EEG sensor space, providing a realistic test bed for algorithmic evaluation and paving the way for future clinical applications. The results showed that existing source localisation approaches performed reasonably well under idealised conditions (343 electrodes, no measurement noise), but their accuracy degraded substantially under more realistic scenarios involving noise and lower-density montages. The primary contributor to this performance

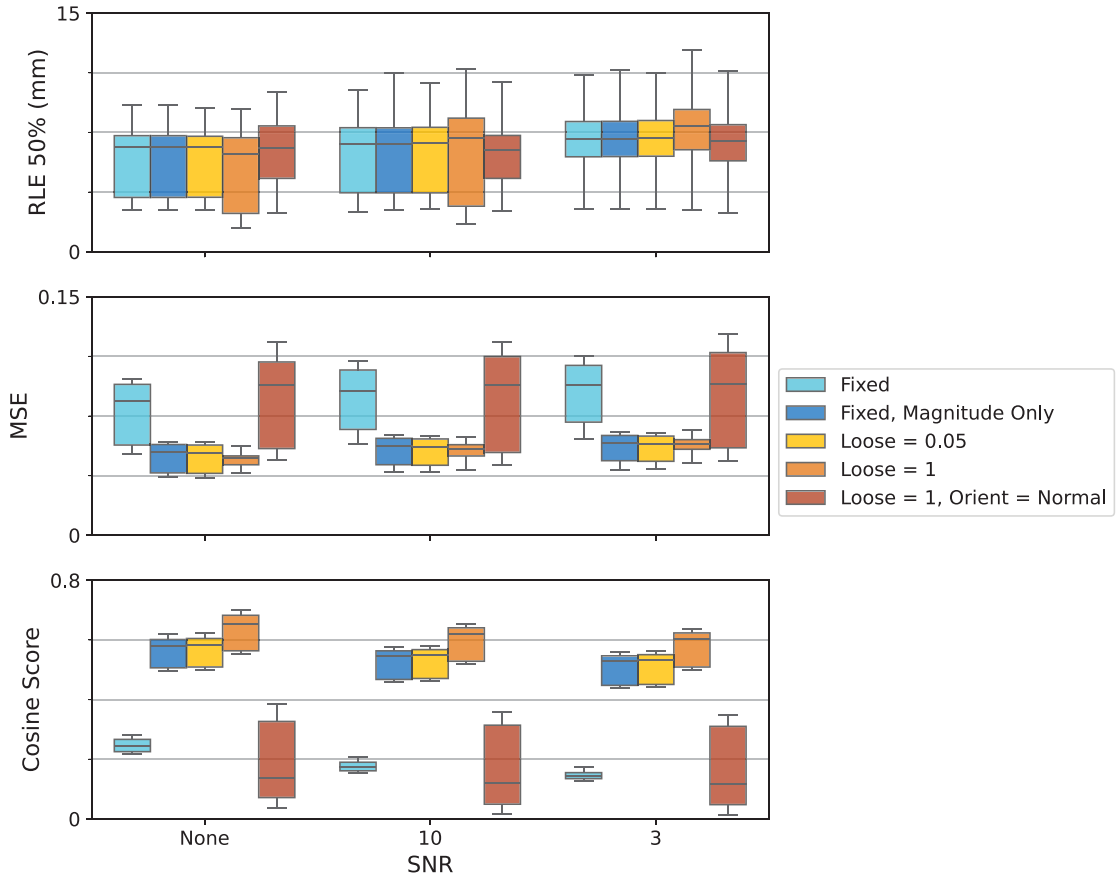

Figure 6. Results of eLORETA when adjusting the loose orientation parameter. Each row is a different metric (region localisation error at 50% EEG power, mean squared error, cosine score), and the *x*-axis indicates the signal-to-noise ratio in dB. Metrics are computed with a 'loose' orientation, which controls the degree to which dipole orientations are allowed to deviate from the normal of the cortical surface. Different loose orientation parameter settings are represented by different colours: Light blue = Fixed orientation, Dark blue = Fixed orientation with taking the absolute value, Gold = Minimally loose orientation (parameter set to 0.05), Orange = Loose orientation, Mahogany = Loose orientation, but taking only the normal to the surface component.

decline was a reduced ability to recover the correct polarity of the underlying sources, even when the spatial localisation itself remained relatively accurate. For the purposes of localising the epileptogenic zone or tracking regional recruitment during seizures, spatial accuracy is typically the dominant consideration. Nonetheless, improving polarity reconstruction remains an important area for future development, particularly for studies concerned with mechanistic insights of seizure dynamics or more generalised hierarchical relations in the brain, as discussed later.

Resolving the polarity of dipole Sources The current results showed that the MN-family of source localisation algorithms was unable to reliably reconstruct the correct polarity of dipole sources under typical EEG conditions, particularly when using lower-density montages. In EEG and MEG source localisation, polarity reflects the orientation of the underlying current dipole relative to the sensors. Although forward models preserve this orientation, inverse solutions often fail to recover it due to the ambiguity of multiple source configurations explaining identical sensor patterns, leading many pipelines to prioritise spatial accuracy over polarity (Gramfort *et al* 2014). For applications such as identifying the epileptogenic zone (or, more broadly, any task focused on where activity originates), spatial precision is indeed far more critical than recovering dipole orientation, especially given susceptibility of polarity to noise, head-model inaccuracies, and orientation ambiguities, as demonstrated in the preceding simulations.

Nevertheless, polarity can carry meaningful physiological information. The polarity represents the direction of current flow across the cortical surface and through the cortical laminae, with implications on the hierarchical (such as feedforward or feedback) relationships between areas in the brain (Ahlfors *et al* 2015, Ahlfors and Wreh 2015, Lankinen *et al* 2024). Polarity may also be essential when interpreting functional connectivity (Haufe and Ewald 2019, Coelli *et al* 2023), phase relationships (Haufe *et al* 2011, Koller *et al* 2024), or propagation direction (Koller *et al* 2024), all of which are vital components of understanding the mechanisms underlying seizures or other generalised wave-like brain activity. Therefore, incorrect signs can invert inferred interactions or misrepresent the temporal

ordering of neural activations. As such, the importance of resolving the correct polarity of the dipole sources should be guided by the scientific or clinical question being asked.

Optimal timing for epileptogenic zone localisation

This study identifies the mid-phase of a seizure, the period following 50% mean global field power, as the optimal time point for EZ localisation (figure 5). This aligns with established interictal practices (Wang *et al* 2011, van Mierlo *et al* 2017), yet appears to contrast with findings by Plummer *et al* (2019), who favoured the early ictal period, as defined by the earliest time point at which 90% of the signal variance could be reconstructed. This discrepancy is primarily methodological. While the 90% variance criterion demands highly regularised, noise-robust inversion, our simulations show that stable localisation under more lenient regularisation emerges between ∼8 s (when the RLE became more stable at each time point) and ∼10 s (the 'elbow' point at which the RLE dropped sharply and began to plateau). Both perspectives suggest that accuracy requires sufficiently organised seizure activity, however, this creates a fundamental clinical trade-off. By the time the signal reaches the stability required for reliable inverse reconstruction, the seizure has typically propagated to secondary regions. Consequently, the clearest reconstruction conditions may spatially misrepresent the underlying pathology by masking the true onset zone with widespread recruitment, reinforcing the necessity of capturing the earliest possible ictal generators.

The selection of ictal intervals for source imaging is further constrained by the onset of physiological noise as the seizure develops. Although the initial seconds of a seizure are typically the least contaminated by gross movement artefacts or EMG activity, the ictal discharge at onset often lacks the signal-to-noise ratio necessary to be distinguished from background neural activity (Cosandier-Rimélé *et al* 2012), accounting for the unstable inverse solutions observed in our results. Conversely, the progression into later ictal phases is frequently accompanied by high-amplitude EMG and movement artefacts, which introduce significant non-neural noise and increase the probability of source localisation errors. Hence, in practice, the identification of an optimal analysis window necessitates a compromise, targeting a period where the ictal rhythm has achieved sufficient amplitude and spatial coherence to be localised but remains prior to the emergence of dominant physiological artifacts or extensive spatial propagation.

Current methods of evaluation Current methods of evaluating source localisation results (as estimated from mesoscopic recordings) can be categorised into three groups:

1. Comparison with simultaneously measured sources,
2. Comparison with empirically inferred sources, and
3. Comparison with simulated sources.

A recent and promising development within the 'simultaneous measurement' category is the availability of datasets that combine simultaneous EEG or MEG with intracranial recordings, such as sEEG (Mikulan *et al* 2020, Pascarella *et al* 2023). These datasets offer a unique opportunity to compare non-invasive estimates with invasive ground truth. For example, Parmigiani *et al* (2022) published an open sEEG dataset based on cortico-cortical evoked potentials from bipolar stimulation. However, to our knowledge, there are currently no published studies that evaluate source imaging approaches with simultaneous invasive and non-invasive measurements of neural activity. Key factors limiting the application of simultaneous recording include technical complexity, restricted spatial coverage with sEEG electrodes, and the presence of stimulation (used to generate clear sources) artefacts dominating both sEEG and EEG signals. Several studies have evaluated techniques using the stimulation artefact itself as the underlying 'source' (Mikulan *et al* 2020, Pascarella *et al* 2023, Unnwongse *et al* 2023), but these are limited to evaluating localisation performance for a single source (the stimulation artefact), which differs from neural activity in terms of amplitude, waveform, and physical origins.

A second strategy involves evaluating the localisation of the epileptogenic zone in patients using empirically inferred sources, either employing surgical outcome as a proxy for ground truth (Plummer *et al* 2019, Sun *et al* 2022) or validating scalp-derived estimates against subsequent intracranial recordings (Koessler *et al* 2010, Pellegrino *et al* 2016). While this approach provides a clinically relevant benchmark, it relies on indirect or temporally separated measurements that introduce inherent validation uncertainties. Specifically, the use of surgical success as a binary outcome measure may bias results in favour of methods that produce larger estimated source volumes, which increases the likelihood of including the true onset zone at the cost of higher false-positive rates. Similarly, the use of sequential intracranial EEG lacks the strict temporal alignment required to ensure that scalp-level signal features correspond to the same underlying neural generators observed in the depth recordings. These combined constraints limit the capacity of current empirical validation methods to resolve the fine-grained spatial-temporal accuracy of source imaging algorithms, particularly during the rapid propagation phase of a seizure.

Finally, the most common benchmarking approach by far has been to simulate the underlying sources directly and apply a forward transformation to obtain a data set with both the underlying sources and the resultant EEG signal (Barzegaran *et al* 2019, Hauk *et al* 2022). This is the approach undertaken by this work, where a clear distinction is the use of biologically-inspired neural mass models to generate the simulations as opposed to relying on a small number of spatially discrete sources (Petrov 2012, Giri *et al* 2022, Cioppa *et al* 2023). This methodology aligns with the realistic modelling framework established by Cosandier-Rimélé *et al* (2017), who systematically evaluated sLORETA performance using biophysically modelled interictal spikes derived from the Wendling neural mass model (Wendling *et al* 2000). While both studies leverage neural population dynamics to provide a rigorous benchmark, the present work extends this approach to the complex, non-stationary dynamics of ictal activity, utilising the Epileptor model in combination with a connectome to evaluate localisation accuracy during seizure evolution and propagation. Consequently, the present study investigates a broader range of source and electrode configurations and provides an analysis of reconstruction polarity. This contrasts with the differing scope of Cosandier-Rimélé *et al* (2017), who focused on a detailed assessment of a subset of interictal spike configurations within the specific constraints of a standard 10–20 clinical montage. Furthermore, while Sun *et al* (2022) have also employed neural mass model simulations, their source localisation algorithm was a deep learning model that was both trained and evaluated on the same simulated environment. No such circularity occurs here.

Limitations and future work While simulations provide valuable ground truth for assessing methodological performance, they inevitably simplify the complexity of real neural dynamics and are unlikely to capture the full range of noise and variability present in real-world data. Specifically, in this work, while the Epileptor model is widely used and is capable of reproducing many spatial and temporal features of epileptic dynamics at both microscale and macroscale levels (Jirsa *et al* 2014, Moosavi *et al* 2022, Wang *et al* 2023), in this implementation, it employs only one of the twelve theoretically defined dynamical transitions associated with seizure initiation and termination (Saggio *et al* 2020). Moreover, assumptions made during simulation design, such as source extent, timescales, and propagation dynamics, may introduce biases in favour of specific modelling approaches. While absolute accuracy in simulation typically overestimates performance in real data, relative performance trends, such as the comparative ranking of methods or the impact of specific parameter adjustments, often generalise (Sargent 2013). Although simulations cannot substitute for clinical validation, in domains such as source localisation, where a definitive ground truth is currently not available, they serve as a critical intermediary, helping to guide expectations, identify limitations, and narrow the space of viable methods prior to clinical deployment. Future work should complement simulation-based evaluation with other forms of real data (such as surgical resection results of epilepsy patients) to verify findings *in vivo*.

A primary limitation of this study is its focus on a single candidate human model. While this approach is sufficient for validating the utility of the neural mass benchmarking framework, it does not account for inter-subject variability. The spatial-temporal dynamics of seizure propagation are highly dependent on the underlying structural connectome and individual anatomical geometry (Moosavi *et al* 2022). Consequently, subject to a relevant hypothesis, future research can use multiple subject templates to investigate how individual differences in brain network topology and head models influence the propagation of pathological activity and the comparative performance of inverse algorithms on such signals. Furthermore, while this work only tested Gaussian measurement noise, clinical recordings are characterised by the presence of biological artefacts, such as myogenic and ocular activity. Expanding the framework to include multiple subjects and biological artefacts will allow for a more robust evaluation of how source localisation methods perform across broader clinical populations and recording conditions.

Due to their established role in clinical practice, this study focused on the evaluation of the minimum-norm family of source localisation algorithms (MNE, dSPM, sLORETA, eLORETA). However, other source imaging techniques exist that possess specific mathematical assumptions that may be advantageous for analysing ictal dynamics. For example, methods that explicitly exploit the rhythmic and oscillatory components characteristic of seizures are relevant, such as dynamic imaging of coherent sources (DICS), which evaluates spatial coherence in the frequency domain (Gross *et al* 2001), and wavelet-based maximum entropy on the mean (wMEM), which utilises time-frequency representations coupled with sparsity constraints (Pellegrino *et al* 2016). Furthermore, spatial filtering techniques, such as linearly constrained minimum variance (LCMV) beamformers (Van Veen *et al* 1997), and signal subspace methods, such as multiple signal classification (MUSIC) (Mosher and Leahy 1998), provide mechanisms for separating true ictal signals from background noise. However, these alternative approaches are also likely to come with specific disadvantages. Beamformers and scanning methods, such as MUSIC, exhibit degraded performance when

sources are highly correlated and temporally synchronous (He *et al* 2018), a common characteristic of rapidly propagating epileptic networks. Sparse reconstruction methods, typically require careful tuning of the sparsity constraint and are prone to over-sparsification leading to overly focused solutions (He *et al* 2018). Furthermore, methods dependent on frequency representations, such as DICS and wMEM, are sensitive to the evolving, non-stationary nature of seizures. Future studies can investigate these algorithms using the proposed benchmarking framework, enabling a quantitative assessment of how their distinct assumptions regarding source correlation, spatial distribution, and rhythmicity balance against their expected mathematical limitations.

Conclusion This study established a benchmarking framework based on biologically inspired neural mass models to evaluate the performance of EEG source localisation algorithms. Using the Epileptor model to generate synthetic seizures, this work provides a realistic testbed that accounts for the complex spatiotemporal dynamics, such as seizure recruitment and propagation, characteristic of clinical epilepsy. The findings obtained through this simulation framework demonstrated that while MN-family algorithms were spatially accurate under idealised conditions, they began to fail under typical clinical environments such as increased measurement noise and lower-density montages. Ultimately, the adoption of neural mass models or other more biophysical simulations for benchmarking source imaging approaches would shift the focus from simple spatial precision to a more nuanced understanding of how source inversion algorithms can represent various dynamical states and regimes in the brain.

Acknowledgments

This research was supported by The University of Melbourne's Research Computing Services, the Petascale Campus Initiative, and an Australian Government Research Training Program (RTP) Scholarship. This research was funded by the Australian Research Council (Discovery Project DP200102600).

Data availability statement

The data cannot be made publicly available upon publication because they are not available in a format that is sufficiently accessible or reusable by other researchers. The data that support the findings of this study are available upon reasonable request from the authors. Structural connectivity data is available from the Human Connectome Project (Van Essen *et al* 2013). Derivative data and code required to reproduce the simulations and analyses are available on Github (Siu 2026).

Conflict of interest

The authors declare that they have no known competing financial interests or personal relationships that could have appeared to influence the work reported in this paper.

Author contributions

Pok Him Siu 0000-0002-6452-495X
Conceptualization (lead), Data curation (equal), Formal analysis (lead), Investigation (lead), Methodology (lead), Software (lead), Validation (lead), Visualization (lead), Writing – original draft (lead), Writing – review & editing (equal)

Philippa J Karoly 0000-0002-9879-5854
Funding acquisition (equal), Investigation (supporting), Methodology (supporting), Supervision (equal), Writing – original draft (supporting), Writing – review & editing (equal)

Sina Mansour L 0000-0002-5695-5696
Data curation (equal), Writing – review & editing (supporting)

Artemio Soto-Breceda 0000-0002-7162-2590
Supervision (equal), Writing – original draft (supporting), Writing – review & editing (equal)

Levin Kuhlmann 0000-0002-5108-6348
Funding acquisition (equal), Writing – original draft (supporting), Writing – review & editing (equal)

Mark J Cook 0000-0002-8875-4135
Formal analysis (supporting), Funding acquisition (equal), Writing – original draft (supporting), Writing – review & editing (equal)

David B Grayden 0000-0002-5497-7234
Funding acquisition (equal), Supervision (equal), Writing – original draft (supporting), Writing – review & editing (equal)

References

Ahlfors S P, Jones S R, Ahveninen J, Hämäläinen M S, Belliveau J W and Bar M 2015 Direction of magnetoencephalography sources associated with feedback and feedforward contributions in a visual object recognition task *Neurosci. Lett.* **0** 149–54

Ahlfors S P and Wreh C 2015 Modeling the effect of dendritic input location on MEG and EEG source dipoles *Med. Biol. Eng. Comput.* **53** 879–87

Bartolomei F, Trébuchon A, Bonini F, Lambert I, Gavaret M, Woodman M, Giusiano B, Wendling F and Bénar C 2016 What is the concordance between the seizure onset zone and the irritative zone? a SEEG quantified study *Clin. Neurophysiol.* **127** 1157–62

Barzegaran E, Bosse S, Kohler P J and Norcia A M 2019 EEGSourceSim: a framework for realistic simulation of EEG scalp data using MRI-based forward models and biologically plausible signals and noise *J. Neurosci. Methods* **328** 108377

Breakspear M 2017 Dynamic models of large-scale brain activity *Nat. Neurosci.* **20** 340–52

Burt J B, Demirtaş M, Eckner W J, Navejar N M, Ji J L, Martin W J, Bernacchia A, Anticevic A and Murray J D 2018 Hierarchy of transcriptomic specialization across human cortex captured by structural neuroimaging topography *Nat. Neurosci.* **21** 1251–9

Cioppa L D, Tartaglione M, Pascarella A and Pitolli F 2023 Solution of the EEG inverse problem by random dipole sampling *Inverse Problems* **40** 025006

Coelli S, Villalon S M, Bonini F, Velmurugan J, López-Madrona V J, Carron R, Bartolomei F, Badier J-M and Bénar C-G 2023 Comparison of beamformer and ICA for dynamic connectivity analysis: A simultaneous MEG-SEEG study *NeuroImage* **265** 119806

Cosandier-Rimélé D, Badier J-M, Chauvel P and Wendling F 2007 A physiologically plausible spatio-temporal model for EEG signals recorded with intracerebral electrodes in human partial epilepsy *IEEE Trans. Biomed. Eng.* **54** 380–8

Cosandier-Rimélé D, Bartolomei F, Merlet I, Chauvel P and Wendling F 2012 Recording of fast activity at the onset of partial seizures: depth EEG vs. scalp EEG *NeuroImage* **59** 3474–87

Cosandier-Rimélé D, Merlet I, Badier J M, Chauvel P and Wendling F 2008 The neuronal sources of EEG: Modeling of simultaneous scalp and intracerebral recordings in epilepsy *NeuroImage* **42** 135–46

Cosandier-Rimélé D, Merlet I, Bartolomei F, Badier J-M and Wendling F 2010 Computational modeling of epileptic activity: from cortical sources to EEG signals *J. Clin. Neurophysiol.* **27** 465

Cosandier-Rimélé D, Ramantani G, Zentner J, Schulze-Bonhage A and Dümpelmann M 2017 A realistic multimodal modeling approach for the evaluation of distributed source analysis: application to sLORETA *J. Neural Eng.* **14** 056008

Costa M S, Born J, Christian Claussen J and Martinetz T 2016 Modeling the effect of sleep regulation on a neural mass model *J. Comput. Neurosci.* **41** 15–28

Dale A M, Liu A K, Fischl B R, Buckner R L, Belliveau J W, Lewine J D and Halgren E 2000 Dynamic statistical parametric mapping *Neuron* **26** 55–67

Desikan R S *et al* 2006 An automated labeling system for subdividing the human cerebral cortex on MRI scans into gyral based regions of interest *NeuroImage* **31** 968–80

Dhollander T, Raffelt D and Connelly A 2016 Unsupervised 3-tissue response function estimation from single-shell or multi-shell diffusion MR data without a co-registered T1 image *ISMRM Workshop on Breaking the Barriers of Diffusion MRI* (*Lisbon*) vol 5

Doelling K B and Assaneo M F 2021 Neural oscillations are a start toward understanding brain activity rather than the end *PLOS Biol.* **19** e3001234

Donald Tournier J, Calamante F and Connelly A 2010 Improved probabilistic streamlines tractography by 2nd order integration over fibre orientation distributions *Proc. Int. Society for Magnetic Resonance in Medicine* vol 1670

Donoghue T *et al* 2020 Parameterizing neural power spectra into periodic and aperiodic components *Nat. Neurosci.* **23** 1655–65

Eguíluz V M, Chialvo D R, Cecchi G A, Baliki M and Apkarian A V 2005 Scale-free brain functional networks *Phys. Rev. Lett.* **94** 018102

Eickhoff S B, Yeo B T T and Genon S 2018 Imaging-based parcellations of the human brain *Nat. Rev. Neurosci.* **19** 672–86

Fischl B 2012 FreeSurfer *NeuroImage* **62** 774–81

Giri A, Kumar L, Kurwale N and Gandhi T K 2022 Anatomical harmonics basis based brain source localization with application to epilepsy *Sci. Rep.* **12** 11240

Glasser M F *et al* 2013 The minimal preprocessing pipelines for the human connectome project *NeuroImage* **80** 105–24

Glasser M F and Van Essen D C 2011 Mapping human cortical areas *In Vivo* based on Myelin content as revealed by T1- and T2-weighted MRI *J. Neurosci.* **31** 11597–616

Gramfort A, Luessi M, Larson E, Engemann D A, Strohmeier D, Brodbeck C, Parkkonen L and Hämäläinen M S 2014 MNE software for processing MEG and EEG data *NeuroImage* **86** 446–60

Gramfort A, Papadopoulo T, Olivi E and Clerc M 2010 OpenMEEG: opensource software for quasistatic bioelectromagnetics *BioMed. Eng. OnLine* **9** 45

Gross J, Kujala J, Hämäläinen M, Timmermann L, Schnitzler A and Salmelin R 2001 Dynamic imaging of coherent sources: studying neural interactions in the human brain *Proc. Natl Acad. Sci.* **98** 694–9

Hallez H *et al* 2007 Review on solving the forward problem in EEG source analysis *J. Neuroeng. Rehabil.* **4** 46

Hämäläinen M S and Ilmoniemi R J 1994 Interpreting magnetic fields of the brain: minimum norm estimates *Med. Biol. Eng. Comput.* **32** 35–42

Haufe S and Ewald A 2019 A simulation framework for benchmarking EEG-based brain connectivity estimation methodologies *Brain Topography* **32** 625–42

Haufe S, Tomioka R, Dickhaus T, Sannelli C, Blankertz B, Nolte G and Müller K-R 2011 Large-scale EEG/MEG source localization with spatial flexibility *NeuroImage* **54** 851–9

Hauk O, Stenroos M and Treder M S 2022 Towards an objective evaluation of EEG/MEG source estimation methods – The linear approach *NeuroImage* **255** 119177

He B, Sohrabpour A, Brown E and Liu Z 2018 Electrophysiological source imaging: a noninvasive window to brain dynamics *Annu. Rev. Biomed. Eng.* **20** 171–96

Hecker L, Rupprecht R, Van Elst L T and Kornmeier J 2021 ConvDip: a convolutional neural network for better EEG source imaging *Front. Neurosci.* **15** 569918

Houssaini K E, Bernard C and Jirsa V K 2020 The epileptor model: a systematic mathematical analysis linked to the dynamics of seizures, refractory status epilepticus and depolarization block *eNeuro* **7** ENEURO.0485-18.2019

Jeurissen B, Tournier J-D, Dhollander T, Connelly A and Sijbers J 2014 Multi-tissue constrained spherical deconvolution for improved analysis of multi-shell diffusion MRI data *NeuroImage* **103** 411–26

Jiang X, Cai Z, Gonsisko C, Worrell G A and He B 2025 Mapping epileptogenic brain using a unified spatial–temporal–spectral source imaging framework *Proc. Natl Acad. Sci.* **122** e2510015122

Jirsa V K *et al* 2017 The virtual epileptic patient: individualized whole-brain models of epilepsy spread *NeuroImage* **145** 377–88

Jirsa V K, Stacey W C, Quilichini P P, Ivanov A I and Bernard C 2014 On the nature of seizure dynamics *Brain* **137** 2210–30

Jirsa V, Wang H, Triebkorn P, Hashemi M, Jha J, Gonzalez-Martinez J, Guye M, Makhalova J and Bartolomei F 2023 Personalised virtual brain models in epilepsy *Lancet Neurol.* **22** 443–454

Karoly P J, Kuhlmann L, Soudry D, Grayden D B, Cook M J and Freestone D R 2018 Seizure pathways: a model-based investigation *PLOS Comput. Biol.* **14** e1006403

Koessler L, Benar C, Maillard L, Badier J-M, Vignal J P, Bartolomei F, Chauvel P and Gavaret M 2010 Source localization of ictal epileptic activity investigated by high resolution EEG and validated by SEEG *NeuroImage* **51** 642–53

Koller D P, M and Ritter P 2024 Human connectome topology directs cortical traveling waves and shapes frequency gradients *Nat. Commun.* **15** 3570

Lankinen K, Ahveninen J, Jas M, Raij T and Ahlfors S P 2024 Neuronal modeling of cross-sensory visual evoked magnetoencephalography responses in the auditory cortex *J. Neurosci.* **44** e1119232024

Leon P S, Knock S A, Woodman M M, Domide L, Mersmann J, McIntosh A R and Jirsa V 2013 The virtual brain: a simulator of primate brain network dynamics *Front. Neuroinformatics* **7** 1662–5196

Lin F-H, Belliveau J W, Dale A M and Hämäläinen M S 2006 Distributed current estimates using cortical orientation constraints *Hum. Brain Mapp.* **27** 1–13

Maran R, Müller E J and Fulcher B D 2025 Analyzing the brain's dynamic response to targeted stimulation using generative modeling *Netw. Neurosci.* **9** 237–58

Mikulan E *et al* 2020 Simultaneous human intracerebral stimulation and HD-EEG, ground-truth for source localization methods *Sci. Data* **7** 127

Moosavi S A, Jirsa V K and Truccolo W 2022 Critical dynamics in the spread of focal epileptic seizures: network connectivity, neural excitability and phase transitions *PLoS One* **17** e0272902

Morik M, Hashemi A, Müller K-R, Haufe S and Nakajima S 2024 Enhancing brain source reconstruction through physics-informed 3D neural networks (arXiv:2411.00143)

Mosher J C and Leahy R M 1998 Recursive MUSIC: a framework for EEG and MEG source localization *IEEE Trans. Biomed. Eng.* **45** 1342–54

Nunez P L 1974 The brain wave equation: a model for the EEG *Math. Biosci.* **21** 279–97

Nunez P L and Srinivasan R 2006 *Electric Fields of the Brain* (Oxford University Press)

Otsu. N 1979 A threshold selection method from gray-level histograms *IEEE Trans. Syst. Man Cybern.* **9** 23–27

Pang J C, Aquino K M, Oldehinkel M, Robinson P A, Fulcher B D, Breakspear M and Fornito A 2023 Geometric constraints on human brain function *Nature* **618** 1–9

Parmigiani S *et al* 2022 Simultaneous stereo-EEG and high-density scalp EEG recordings to study the effects of intracerebral stimulation parameters *Brain Stimul.* **15** 664–75

Pascarella A *et al* 2023 An in–vivo validation of ESI methods with focal sources *NeuroImage* **277** 120219

Pascual-Marqui R D 2007 Discrete, 3D distributed, linear imaging methods of electric neuronal activity. Part 1: exact, zero error localization (available at: https://arxiv.org/abs/0710.3341)

Pascual-Marqui R D, Esslen M, Kochi K and Lehmann D 2002 Functional imaging with low-resolution brain electromagnetic tomography (LORETA): a review *Methods Findings Exp. Clin. Pharmacol.* **24** 91–95

Pellegrino G, Hedrich T, Chowdhury R, Hall J A, Lina J-M, Dubeau F, Kobayashi E and Grova C 2016 Source localization of the seizure onset zone from ictal EEG/MEG data: wMEM for Ictal source imaging *Hum. Brain Mapp.* **37** 2528–46

Petrov Y 2012 Harmony: EEG/MEG linear inverse source reconstruction in the anatomical basis of spherical harmonics *PLoS One* **7** 44439

Plummer C, Vogrin S J, Woods W P, Murphy M A, Cook M J and Liley D T J 2019 Interictal and ictal source localization for epilepsy surgery using high-density EEG with MEG: a prospective long-term study *Brain* **142** 932–51

Rong J, Sun R, Joseph B, Worrell G and He B 2025 Deep learning-based EEG source imaging is robust under varying electrode configurations *Clin. Neurophysiol.* **175** 2010730

Saggio M L *et al* 2020 A taxonomy of seizure dynamotypes *eLife* **9** e55632

Saggio M L and Jirsa V 2024 Bifurcations and bursting in the Epileptor *PLOS Comput. Biol.* **20** e1011903

Sanz-Leon P, Knock S A, Spiegler A and Jirsa V K 2015 Mathematical framework for large-scale brain network modeling in the virtual brain *NeuroImage* **111** 385–430

Sargent R G 2013 Verification and validation of simulation models *J. Simul.* **7** 12–24

Sharma P, Seeck M and Beniczky S 2019 Accuracy of interictal and ictal electric and magnetic source imaging: a systematic review and meta-analysis *Front. Neurol.* **10** 1664–2295

Sina Mansour L, Di Biase M A, Smith R E, Zalesky A and Seguin C 2023 Connectomes for 40,000 UK Biobank participants: a multi-modal, multi-scale brain network resource *NeuroImage* **283** 120407

Sina Mansour L, Tian Y, Thomas Yeo B T, Cropley V and Zalesky A 2021 High-resolution connectomic fingerprints: mapping neural identity and behavior *NeuroImage* **229** 117695

Siu P H 2026 Spokhim/sl_sim_framework *Github* (available at: https://github.com/Spokhim/sl_sim_framework)

Siu P H, Müller E, Zerbi V, Aquino K and Fulcher B D 2022 Extracting dynamical understanding from neural-mass models of mouse cortex *Front. Comput. Neurosci.* **16** 1662–5188

Smith R E, Tournier J-D, Calamante F and Connelly A 2012 Anatomically-constrained tractography: improved diffusion MRI streamlines tractography through effective use of anatomical information *NeuroImage* **62** 1924–38

Sohrabpour A, Cai Z, Ye S, Brinkmann B, Worrell G and He. B 2020 Noninvasive electromagnetic source imaging of spatiotemporally distributed epileptogenic brain sources *Nat. Commun.* **11** 1946

Sotero R C, Trujillo-Barreto N J, Iturria-Medina Y, Carbonell F and Jimenez J C 2007 Realistically coupled neural mass models can generate EEG rhythms *Neural Comput.* **19** 478–512

Sun R, Sohrabpour A, Joseph B, Worrell G and He. B 2024 Seizure sources can be imaged from scalp EEG by means of biophysically constrained deep neural networks *Adv. Sci.* **11** 2405246

Sun R, Sohrabpour A, Worrell G A and He. B 2022 Deep neural networks constrained by neural mass models improve electrophysiological source imaging of spatiotemporal brain dynamics *Proc. Natl Acad. Sci.* **119** e2201128119

Tournier J-D, Smith R, Raffelt D, Tabbara R, Dhollander T, Pietsch M, Christiaens D, Jeurissen B, Yeh C-H and Connelly A 2019 MRtrix3: a fast, flexible and open software framework for medical image processing and visualisation *NeuroImage* **202** 116137

Unnwongse K, Rampp S, Wehner T, Kowoll A, Parpaley Y, von Lehe M, Lanfer B, Rusiniak M, Wolters C and Wellmer J 2023 Validating EEG source imaging using intracranial electrical stimulation *Brain Commun.* **5** 023

Van Essen D C, Smith S M, Barch D M, Behrens T E J, Yacoub E and Ugurbil K 2013 The WU-Minn human connectome project: an overview *NeuroImage* **80** 62–79

van Mierlo P *et al* 2017 Automated long-term EEG analysis to localize the epileptogenic zone *Epilepsia Open* **2** 322–33

van Mierlo P, Vorderwülbecke B J, Staljanssens W, Seeck M and Vulliémoz S 2020 Ictal EEG source localization in focal epilepsy: review and future perspectives *Clin. Neurophysiol.* **131** 2600–16

Van Veen B D, Van Drongelen W, Yuchtman M and Suzuki A 1997 Localization of brain electrical activity via linearly constrained minimum variance spatial filtering *IEEE Trans. Biomed. Eng.* **44** 867–80

Wang G, Worrell G, Yang L, Wilke C and He. B 2011 Interictal spike analysis of high density EEG in patients with partial epilepsy *Clin. Neurophysiol.* **122** 1098–105

Wang H E et al 2023 Delineating epileptogenic networks using brain imaging data and personalized modeling in drug-resistant epilepsy *Sci. Trans. Med.* **15** eab8982
Wendling F, Bartolomei F, Bellanger J J and Chauvel P 2002 Epileptic fast activity can be explained by a model of impaired GABAergic dendritic inhibition *Eur. J. Neurosci.* **15** 1499–508
Wendling F, Bellanger J J, Bartolomei F and Chauvel P 2000 Relevance of nonlinear lumped-parameter models in the analysis of depth-EEG epileptic signals *Biol. Cybern.* **83** 367–78
Yan X et al 2023 Homotopic local-global parcellation of the human cerebral cortex from resting-state functional connectivity *NeuroImage* **273** 120010
Ying T, Burkitt A N and Kameneva T 2023 Combining the neural mass model and Hodgkin–Huxley formalism: Neuronal dynamics modelling *Biomed. Signal Process. Control* **79** 104026